Research article

Optimizing microstructure, shrinkage defects and mechanical performance of ZL205A alloys via coupling travelling magnetic fields with unidirectional solidification

Lei Luo [a,*], Liangshun Luo [a], Yanqing Su [a,*], Lin Su [b], Liang Wang [a], Jingjie Guo [a], Hengzhi Fu [a]

[a] *National Key Laboratory for Precision Hot Processing of Metals, School of Materials Science & Engineering, Harbin Institute of Technology, Harbin 150001, China*
[b] *Office of International Cooperation, University of Science and Technology of China, Hefei 230026, China*

ABSTRACT

ZL205A alloys tend to form disordered and defective microstructure due to the large solidification intervals and multi-phase. Accordingly, finding ways to effectively optimize the microstructure and mechanical performance is of great significance. In this regard, the coupling of travelling magnetic fields (TMF) with unidirectional solidification was used to continuously regulate the mushy zones of ZL205A alloys. Additionally, experiments are combined with simulations to systematically reveal the mechanisms on the optimizations at each stage of solidification process. Current findings demonstrate that different directional strong melt flows generated by TMF are responsible for these optimizations. Additionally, the effects of TMF on microstructure are different at each stage of solidification process. Specifically, downward TMF coupled with unidirectional solidification can refine and uniform the microstructure, decrease the formation of precipitation, promote the growth consistency of matrix phase α-Al growing along the <001> crystal orientation, reduce the secondary dendrites and overlaps between dendrites, eliminate the shrinkage defects, and increase the ultimate tensile strength, yield strength, elongation and hardness from 198.3 MPa, 102.2 MPa, 7.5 % and 82.3 kg mm^{-2} without TMF to 225.5 MPa, 116.1 MPa, 13.6 % and 105.2 kg mm^{-2}. Contrastively, although upward TMF can reduce Al$_3$Ti and refine α-Al, it increases the formation of Al$_6$Mn, Al$_2$Cu, secondary dendrites, overlaps between dendrites, and shrinkage defects; then it deflects and disorders the growth of α-Al, further to decrease the overall performance of alloys.

© 2020 Published by Elsevier Ltd on behalf of The editorial office of Journal of Materials Science & Technology.

Introduction

Currently, the large solidification intervals of alloys, i.e., the difference between the liquid and solid temperatures, are prone to inducing the unstable solid-liquid interface and serious compositional undercooling in mushy zones [1–3], leading to the deflected and disordered growth of microstructure, accompanied with the prolific formation of secondary dendrites and overlaps between dendrites [4]. In this case, the feeding channels between dendrites in the mushy zones are easily blocked, which can restrict the melt flows, reduce the feeding capacity, and increase the generation of shrinkage, pores and segregation defects [5]. The ZL205A alloys is

an Al-Cu-based alloys extensively employed in the automobiles, aerospace, aviation and military fields [6], due to the outstanding comprehensive mechanical properties including the low density, high specific strength, ductility and toughness [7– 9]. Because ZL205A alloys not only has the large solidification intervals, but also is a multi-element alloys with multi-phase and more complicated solidification behavior produced in the solidification process, it will be more inclined to aggrandize the formation of defects [10] and easily exert negative impacts on the microstructure and mechanical performance of castings [11,12]. Therefore, by comprehensively considering both the large solidification intervals and multi-phase in the solidification process, finding ways to effectively optimize together the microstructure and defects, further to enhance the mechanical properties, is of great significance. In this regard, many methods have been proposed from the perspective of microstructural optimization, such as, adding the refiners [13], increasing the
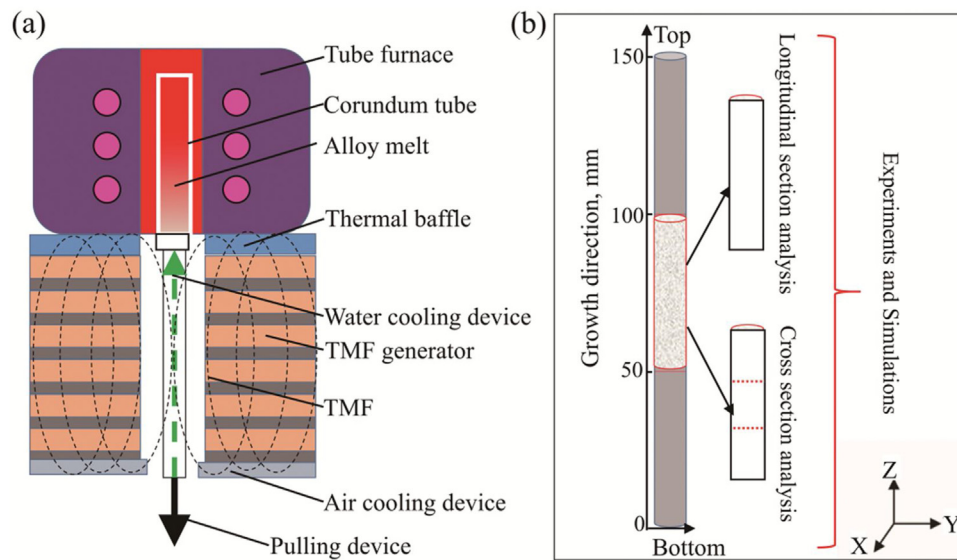
Fig. 1. Schematic diagrams of experiment and the selection of samples: (a) TMF process equipment with unidirectional solidification function. (b) The selection of samples for experiments and simulations [27].

cooling rate [14,15], and performing ultrasonic treatments or external physical fields [16–19]. In addition, many approaches have been used to remove the defects, such as changing the gating system [20], altering the casting modes [21] and regulating the melt condition [22,23], as well as applying external physical fields [16,17]. Contrastively, travelling magnetic fields (TMF) is a more attractive means with pollution-free, contactless and controllability [24], which can achieve the optimization of both the microstructure and the defects at the same time [25,26]. In the current research results [27], it has been confirmed that, for Al-5 wt.% Cu alloys model, i.e., a binary alloys, downward TMF coupling with sequential solidification process is conducive to obtaining the homogenized and refined microstructure growing along the direction of temperature gradient, due to the strong long-range and directional melt flows induced by TMF. Additionally, other literatures have also indicated that TMF can break the secondary dendrite arms to reduce the overlaps between dendrites [28,29], in turn to effectively penetrate the mushy zone, so as to improve the feeding capacity, eliminate the shrinkage defects [30,31], and influence the performance of alloys [32,33]. However, at present, the specific approach to optimize the microstructure and performance of multi-element ZL205A alloys are rare, due to the large solidification intervals and multiphase. Furthermore, the systematic studies about effects of TMF on the microstructural evolution, the elimination of defects and the improvement of mechanical performance of ZL205A alloys are unclear and incomplete. Moreover, the related mechanisms of TMF on ZL205A alloys with large solidification intervals and multi-phase remain systematically unexplained, as well as the relationships among the microstructure, defects and performance.

To this end, based on previous research, in the current work, the coupling of TMF with unidirectional solidification is performed to optimize the microstructure, shrinkage defects and mechanical performance of ZL205A alloys with large solidification intervals and multi-phase. Furthermore, by combining experiments and simulations, the effects of different directional TMF on microstructure at each stage of solidification process, as well as the shrinkage defects and the mechanical properties are systematically studied. The aim is to establish an effective method to optimize together the microstructure, shrinkage defects and mechanical performance of ZL205A alloys, further to fully illustrate the mechanism for the positive optimization induced by the TMF process, as well as the

relationships among the microstructure, the shrinkage defects and the mechanical performance.

Methods

Material preparation

The ZL205A alloy samples (Al-5.0 wt.% Cu-0.3 wt.% Mn-0.15 wt.% Ti) were prepared by a self-designed TMF processing equipment with unidirectional solidification function as shown in Fig. 1(a). The intensity of magnetic fields in equipment was controlled by the alternating excitation current. In order to be closer to the conditions of industrial production, the frequency of 50 Hz was adopted for the alternating excitation current. Moreover, according to the current findings [27], the intensity of 20A was selected for the alternating excitation current to make a comparative study on the multiphase alloys on this basis. In addition, the temperature gradient G_T and cooling rate v_c measured by several times were 3 K mm^{-1} and 0.5 K s^{-1} during the unidirectional solidification process. In addition, the "Up-TMF", "Down-TMF" and "No-TMF" denote the solidification process with upward axial magnetic force, with downward axial magnetic force and without TMF respectively. Because of the strong spatial and temporal dependence of TMF [30], the alloy melt was pulled downward with a constant velocity v_d = 167 μm s^{-1} to maintain the mushy zones in the effective region of TMF, which was given by:

$$v_d = v_c/G_T \qquad (1)$$

Each ZL205A alloy sample was melted at 1023 K in a resistance furnace and degassed with high-purity argon. After holding for 15 min, the alloy melt was poured into a corundum tube with 10 mm in diameter and 150 mm in length. The corundum tube was preheated in the tube furnace at 1023 K (Fig. 1(a)), where the unidirectional solidification process, with or without TMF, was carried out.

Measurement and analysis methods

As shown in Fig. 1(b), a location between 50 and 100 mm from the bottom to the top of samples along the growth direction was selected and cut in half evenly along the longitudinal direction, to analyze their microstructure on the transverse and

Table 1
Related characteristics of the TMF generator and the parameters used in the simulations of TMF and flow fields [34,35].

Parameters	Symbol	Value
TMF inner diameter	D_i, mm	40
TMF outer diameter	D_o, mm	140
Number of windings	n	600
Current frequency	f, Hz	50
Phase sequence	–	Down-TMF: 0, $2\pi/3$, $4\pi/3$; Up-TMF: $4\pi/3$, $2\pi/3$, 0
Excitation current intensity	I_e, A	20
Temperature gradient	G_T, K mm^{-1}	3
Cooling rate of alloys	v_c, K s^{-1}	0.5
Thermal Conductivity	C_T, W mK^{-1}	136
Magnetic permeability	μ_{Al}, H m^{-1}	1.0
Viscosity coefficient	η, Pa s	1.25e-3
Electrical conductance	σ, S m^{-1}	35.33e+6
Latent heat	L_m, kJ kg^{-1}	396.09

the longitudinal sections by using scanning electron microscopy (SEM, Quanta 200FEG, FEI, USA). The chemical composition of the phases in the microstructure was determined by the combination of energy dispersive spectroscopy (EDS, Quanta 200FEG, FEI, USA), X-ray diffraction (XRD, Empyrean, Panalytical, NL) and X-ray photoelectron spectroscopy (XPS, ESCALAB 250Xi, ThermoFisher, USA). In addition, the electron back-scattered diffraction (EBSD, Quanta 200FEG, FEI, USA) and Image-Pro software (Media Cybernetics, Inc., USA) were used together to measure and calculate the crystal orientation and the volume fraction of the precipitates, as well as the size of the dendrites and shrinkage defects. What is noteworthy is that the functions of SEM, EDS and EBSD were implemented on the same instrument. Moreover, the tensile properties were tested for 6 times to take the average values (the standard deviation was about 5 %) for each sample by using the universal testing machine (Instron5569, Instron, USA) at room temperature with a strain rate of 10^{-3} s^{-1}. Naturally, the tensile axis was chosen parallel to the direction of temperature gradient. Similarly, micro-hardness were measured for 30 times to pick the average (the standard deviation was approximately 5 %) by using the hardness tester (HVS-1000A, Laizhou Huayin, CHN) with a 500 g load and a dwell time of 10 s. The density tests of samples were conducted by a high precision digital display density meter (QL-202GR, Shenzhen Qunlong, CHN), and the average of 20 times measurements was selected, of which the standard deviation was about 5 %. The intensity of the magnetic fields used in the experiments was measured by using a tesla-meter (HT201A, Shanghai Hengtong, CHN).

Simulations and calculations

ZL205A alloys phase diagrams were calculated by Pandat software (CompuTherm LLC, USA). The magnetic fields and magnetic force were simulated by Ansoft-Maxwell software (ANSYS Inc., USA). Besides, the melt flows generated by TMF were emulated by Ansoft-CFX software (ANSYS Inc., USA). In the simulations, the following assumptions were made: (i) the heating caused by TMF were not considered in the simulations; (ii) the initial mushy zone was simplified as the T_m =821 K isothermal region between 30– 35 mm from the bottom of samples along the growth direction; (iii) in the boundary conditions, the initial lowest temperature (at the bottom) and the initial highest temperature (at the top) were set as 600 K and 1050 K respectively; (iv) the magnetic forces were assumed to be only applied to the melt with temperatures above, or equal to, T_m. Besides, the related experimental and simulated parameters are shown in Table 1 [34,35].

Results

With respect to the study on ZL205A alloys, the research focused on the variations of microstructure (including the precipitation phases and matrix phase α-Al [36– 38]), shrinkage defects and mechanical performance induced by TMF.

Evolution of precipitates in microstructure

The evolution of precipitates is mainly due to the formation, morphology and distribution in the microstructure, so that the SEM and EDS analysis were first performed on the longitudinal and cross section of samples as shown in Fig. 2 and Table 2. Therefore, the results illustrate that without the TMF process, many precipitation phases including the Al$_3$Ti (Point 1,8), Al$_6$Mn (Point 2) and Al$_2$Cu (Point 3) appear in the microstructure on both the cross and longitudinal sections of alloy samples (Fig. 2(a), (d), (g) and (j)). Moreover, the Al$_3$Ti aggregates and forms the blocky morphology with large size. Meanwhile, the Al$_6$Mn phase distributes adhere to the Al$_2$Cu, resulting in a combination of Al$_6$Mn and Al$_2$Cu. This combined microstructure distributes mainly along the grain boundaries of matrix α-Al. While, by adding the Up-TMF process, the precipitation phases are still mainly the isolated distributed Al$_3$Ti (Point 4) and a combination of Al$_3$Ti (Point 10), Al$_6$Mn (Point 9) and Al$_2$Cu (Points 5,11). However, the size of Al$_3$Ti (Point 4) with blocky morphology decreases on the longitudinal section, while blocky morphological Al$_3$Ti phase with large size are rare on the transverse section of alloy samples (Fig. 2(b),(e), (h) and (k)). Furthermore, the Al$_3$Ti phase (Point 10) with a small size appears around the Al$_2$Cu and the Al$_6$Mn. As a result, a new combined microstructure of Al$_3$Ti, Al$_6$Mn and Al$_2$Cu can be formed along the grain boundaries of matrix α-Al in alloys. Noteworthily, when the Down-TMF is applied, the blocky morphological Al$_3$Ti phase is no longer appearing in the microstructure on both transverse section and longitudinal section of alloy samples (Fig. 2(c), (f), (i) and (l)). Besides, Al$_3$Ti phase with any shape are almost nonexistent around the Al$_2$Cu phase. Additionally, the Al$_6$Mn phase begins to decrease or even disappear after the Down-TMF process. Consequently, in this case, the precipitation phase mainly is the Al$_2$Cu (Points 6, 7, 13) accompanied with a little Al$_6$Mn phase (Point 12).

To further verify the composition of the precipitated phase, XRD measurements were carried out for both the transverse section and longitudinal section of alloy samples, and the statistics for the volume fraction of precipitation phase were performed by using EBSD tests. The results shown in Fig. 3 explicitly indicate that the TMF process can effectively influence the formation of precipitated phase. Specially, by combining the results in Table 2 and Fig. 3, in the unidirectional solidification without the TMF process, the microstructure is mainly the α-Al, Al$_3$Ti, Al$_6$Mn and Al$_2$Cu phases. However, when the Up-TMF is added, the diffraction peak of Al$_3$Ti decreases relatively (Fig. 3(b)), while, leading to an increase of the diffraction peak of Al$_6$Mn and Al$_2$Cu. In addition, by adding the Down-TMF process, the diffraction peak of Al$_3$Ti, Al$_6$Mn and Al$_2$Cu are all decreased largely or even eliminated. Moreover, according to the statistical results about the total volume fraction of precipitated phases (Fig. 3(c)), it has been demonstrated that the Down-TMF process can efficaciously restrict the growth and formation of precipitated phases, and greatly reduce the total volume fraction and size of them. Oppositely, Up-TMF increases the total volume fraction of precipitated phases, although it can decrease the quantity and the size of Al$_3$Ti.

Evolution of the matrix phase α-Al

Similarly, the evolution of matrix phase α-Al are lie in the growth behavior and morphology of them. Similarly, the EBSD measure-
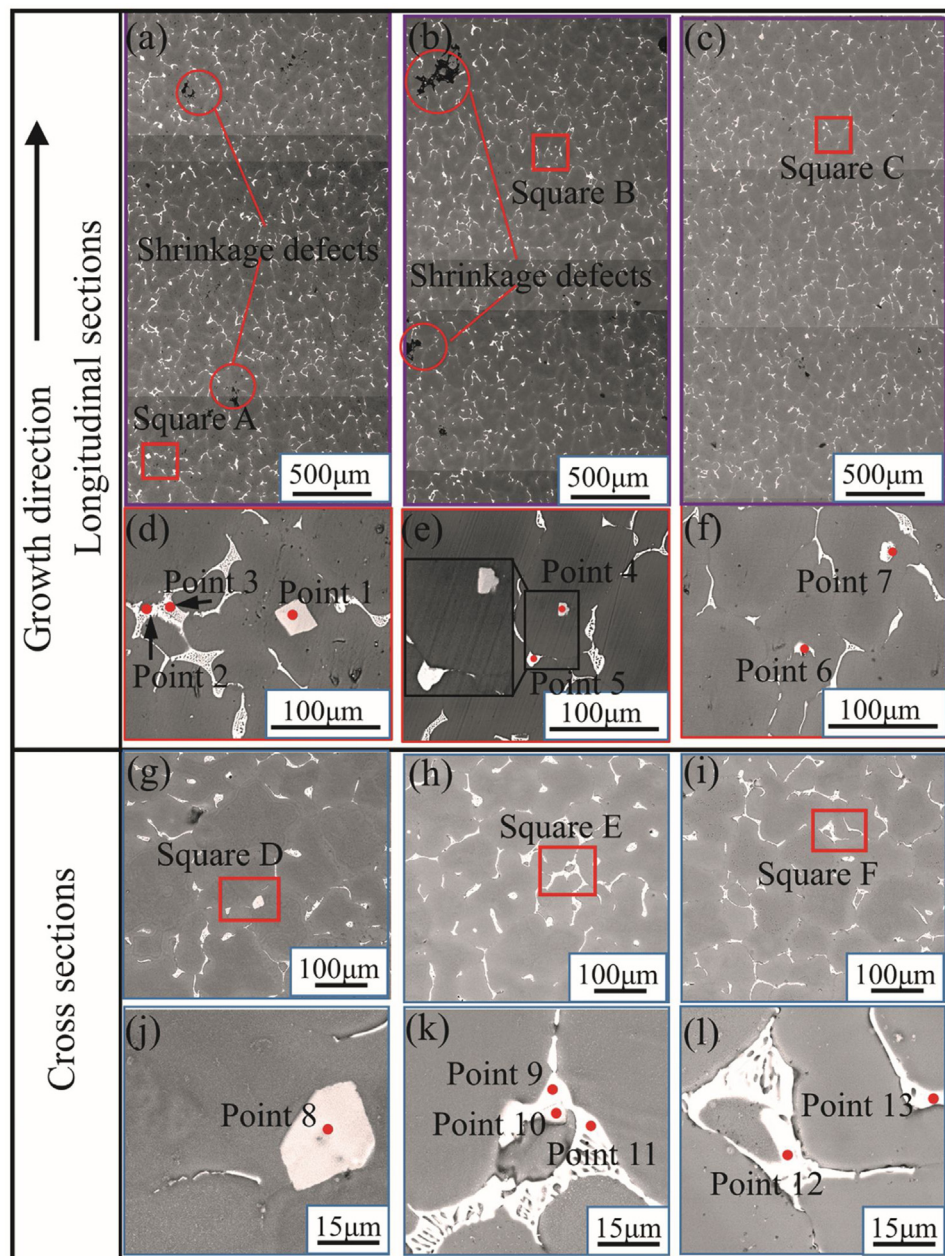
Fig. 2. SEM images of alloy samples: (a), (b) and (c) are the longitudinal sections by No-TMF, Up-TMF and Down-TMF, respectively. (d), (e) and (f) are the locally enlarged images for Square A, B and C, respectively. (g), (h) and (i) are the cross sections by No-TMF, Up-TMF and Down-TMF, respectively. (j), (k) and (l) are the locally enlarged images for Square D, E and F, respectively. (Note: Point denotes energy spectrum point).

ments on matrix phase α-Al was performed as shown in Fig. 4. From the <001>- pole figures and the <001>- inverse pole figures demonstrated in Fig. 4, it is apparent that the crystal orientations of matrix phase α-Al are mainly the <001>, whether in the processes without TMF, with Up-TMF or a Down-TMF. While, when the TMF is absent, there are some deflections of <001> crystal orientation as shown in Fig. 4(a1). Contrastively, However, the addition of Up-TMF obviously reduces the proportion of the <001> crystal orientation to some extent, instead, it results in some specific directions for the growth of matrix phase α-Al as demonstrated in Area A of Fig. 4(b1). However, by adding the Down-TMF process, the <001> crystal orientation of matrix phase α-Al can be greatly promoted (Fig. 4(c1)). In addition, from Fig. 3(a), it can also be obtained that the diffraction peak of matrix phase α-Al at $(200)_{Al}$ and $(111)_{Al}$ crystal planes are higher than other crystal planes in the process

without TMF. However, the diffraction peak of matrix phase α-Al is decreased at $(200)_{Al}$ crystal planes but increased at $(111)_{Al}$ crystal planes by the Up-TMF process. Inversely, it will be increased at $(200)_{Al}$ crystal planes but decreased at $(111)_{Al}$ crystal planes with the Down-TMF process. In other words, Down-TMF promotes the growth of matrix phase α-Al along the <001> crystal orientation comparing to the No-TMF process, while the Up-TMF causes the matrix phase α-Al to grow away from the <001> crystal orientation. Additionally, from Fig. 4(d), it can be indicated that without the TMF process, there are numbers of large mis-orientation angles (the number fraction of 60.2 degrees is about 8.9 %) appearing in the matrix phase α-Al, which means that the growth direction of them are inconsistent and disordered. In this case, the morphology of matrix phase α-Al are irregular in the microstructure, meanwhile, the secondary dendrite and the overlaps between dendrite are pro-

moted (Fig. 4(a3)), leading to a large grain size of matrix phase α-Al, of which the maximum value is 199.3 μm (Fig. 4(e)). With the Up-TMF process (Fig. 4(d)), the number fraction of large mis-orientation angles (such as 60.2 degrees) increases to 10.1 %, and the small mis-orientation angles (such as 3.5 degrees) also increases from 44.1 % (No-TMF) to 54.2 % (Up-TMF), which clearly demonstrates that the matrix phase α-Al under the Up-TMF process tends to form extreme growth in two directions. In addition, the secondary dendrite and the overlaps between dendrite can be more easily increased (Fig. 4(b3)). However, the grain size of matrix phase α-Al decreases, of which the maximum value is 129.0 μm (Fig. 4(e)). Contrastively, by the Down-TMF process, the volume fraction of large mis-orientation angles (such as 60.2 degrees) decreases to 2.0 %, while the low mis-orientation angles (such as 3.5 degrees) increases to 60.2 % (Fig. 4(d)), which means that the growth direction of matrix phase α-Al is more consistent by the addition of Down-TMF. Under this condition, the secondary dendrite and the overlaps between dendrite can be effectively reduced, so that the morphology and distribution of matrix phase α-Al are more uniform (Fig. 4(c3)), of which the grain size is greatly decreased (the maximum value is 111.3 μm) as shown in Fig. 4(e).

Overall, the Down-TMF effectively promotes the growth consistency of matrix phase α-Al growing along with the <001> crystal orientation in ZL205A alloys with large solidification intervals and multi-phase, and reduces the formation of secondary dendrite and the overlaps between dendrite, further to significantly uniform and refine the matrix phase α-Al. However, the Up-TMF declines the growth consistency of α-Al, causes the growth of α-Al to deflect away from <001> crystal orientation, and promotes the formation of secondary dendrite and overlaps between dendrite, although it can decrease the grain size of matrix phase α-Al.

Variation of the shrinkage defects

Since the solidification process has a reasonable degassing process, the defects are more likely to be caused by shrinkage in the microstructure rather than by gas. In this regard, TMF can alter the

Table 2
EDS results for each energy spectrum point in Fig. 2 (at.%).

Point number	Al	Cu	Ti	Mn
1	81.41	0.98	16.75	0.86
2	83.46	8.83	0.01	7.70
3	72.25	27.15	0.27	0.33
4	83.39	0.57	14.86	1.18
5	64.64	34.95	0.10	0.31
6	68.06	31.49	0.18	0.27
7	73.61	25.78	0.28	0.34
8	83.28	0.51	15.38	0.83
9	81.81	9.03	0.10	9.06
10	83.03	0.73	15.07	1.17
11	68.96	30.38	0.25	0.41
12	71.21	25.96	0.32	2.51
13	71.02	28.53	0.19	0.26

solidification behavior and the feeding capacity of ZL205A alloy melt during the unidirectional solidification, so as to influence the formation and distribution of shrinkage defects. Therefore, as shown in Fig. 2(a)– (c), the shrinkage defects were marked by the red circles and measured the size of them by the Image-Pro software. Additionally, the porosities of alloys were calculated by using the equation [39]:

$$P_p = 1 - \rho_s / \rho_0, \tag{2}$$

where the P_p denotes the porosity of alloy samples caused by shrinkage defects, the ρ_s is the average density of the alloy castings taken by several times measurements, and the ρ_0 is the theoretical density of alloys. It can be obvious that without the TMF process, many shrinkage defects occur at grain boundaries of matrix phase α-Al in the microstructure (Fig. 2(a)) and the porosity is 1.81 %, due to the large solidification intervals of ZL205A alloys. In this case, the distribution of shrinkage defects is relatively random, and the maximum size of their length is 55.1 μm. However, when Up-TMF is added into the unidirectional solidification process, the shrinkage defects begin to accumulate, of which the maximum size increases to 373.9 μm (Fig. 2(b)). Finally, the porosity increases to 2.32 % with
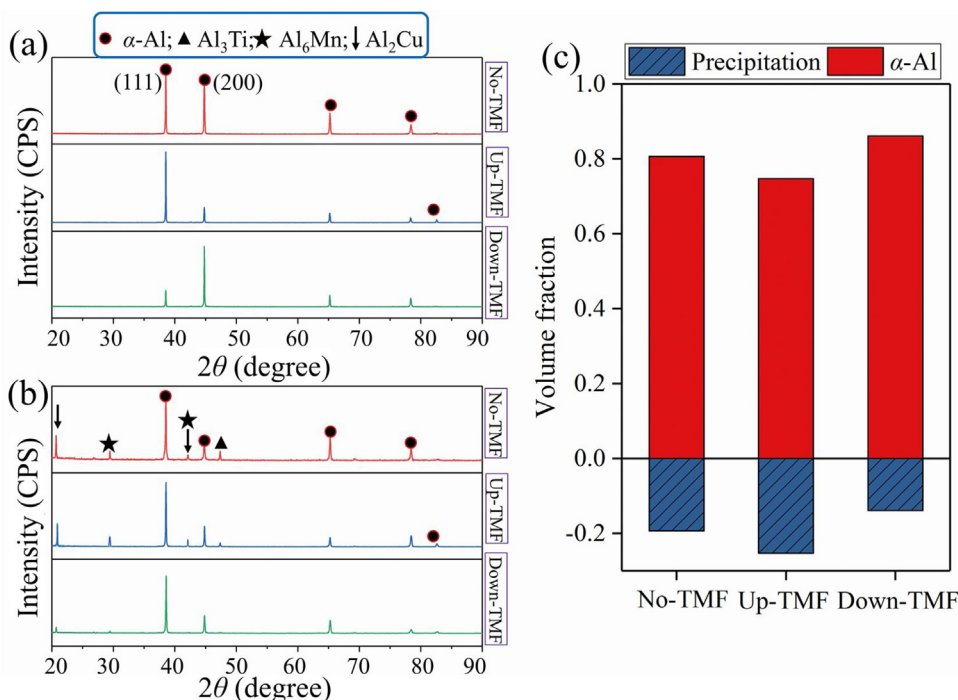

Fig. 3. The composition and content of precipitation phases: (a) and (b) are XRD maps of the cross and longitudinal sections, respectively. (c) The volume fraction of precipitation phase measured by EBSD.
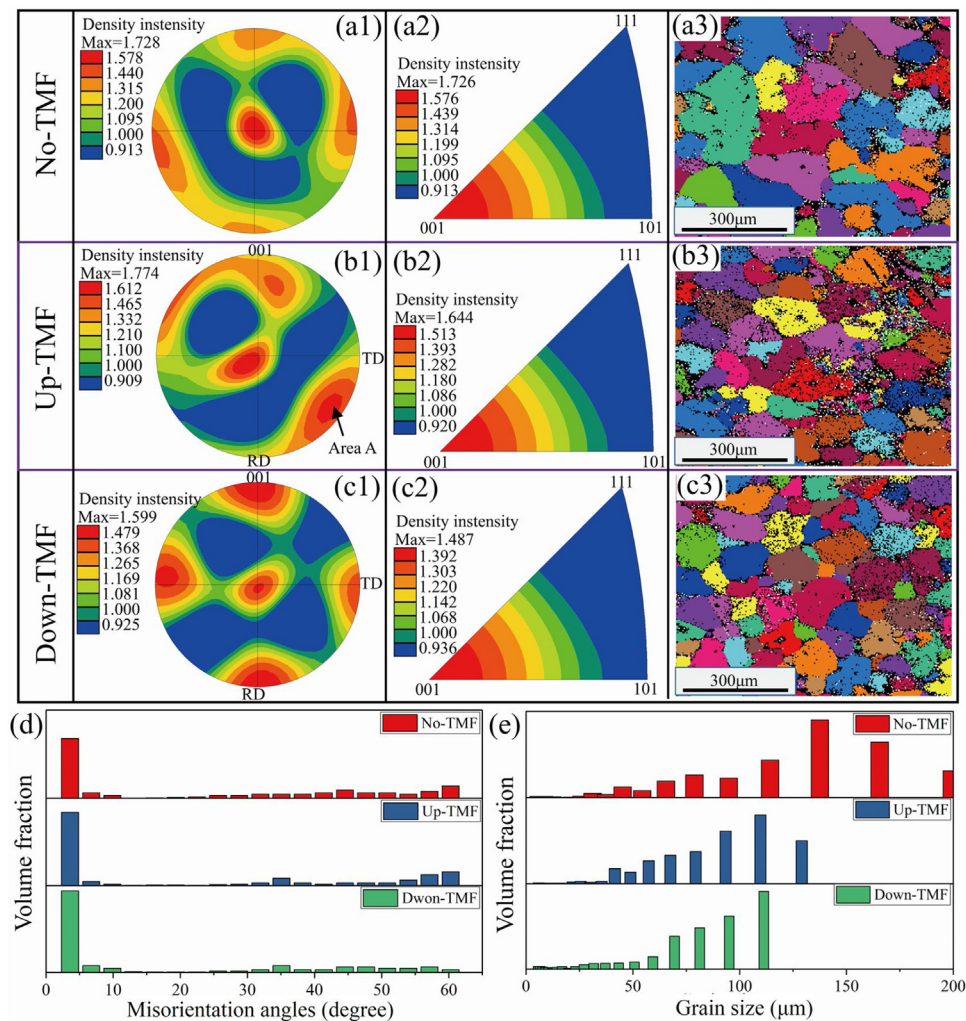
Fig. 4. Statistical results of α-Al phase determined by EBSD: (a1), (b1) and (c1) are the <001>- pole figures. (a2), (b2) and (c2) are the <001>-inverse pole figures. (a3), (b3) and (c3) are the grain figures. (d) Misorientation angles of α-Al phase. (e) Grain size of α-Al phase.

the Up-TMF process. Contrastively, the addition of Down-TMF can significantly reduce the size and formation of shrinkage defects in the microstructure (Fig. 2(c)). Hence, the maximum size and porosity of alloys with the Down-TMF process decrease to 13.1 μm and 0.33 % respectively.

Variations in mechanical properties of alloys

Current findings [40,41] have suggested that the variation of microstructure will directly affect the mechanical properties of alloys. Therefore, the mechanical performance of ZL205A alloy, including the tensile strength and micro-hardness, were tested, and the fracture surface behavior of samples were analyzed. The performance results demonstrated in Fig. 5(a) indicate that, compared with the solidification process without TMF, the Down-TMF can effectively improve the mechanical performance of alloys, especially, it can increase the ultimate tensile strength, yield strength, elongation and the micro-hardness from 198.3 MPa, 102.2 MPa, 7.5 % and 82.3 kg mm^{-2} (without TMF process) to 225.5 MPa, 116.1 MPa, 13.6 % and 105.2 kg mm^{-2} (with Down-TMF process). Contrastively, Up-TMF produced negative effects on mechanical performance. Specifically, it will decrease the ultimate tensile strength, yield strength and elongation to 180.5 MPa, 86.9 MPa and 7.3 %, although it can increase the micro-hardness to 87.2 kg mm^{-2}. Furthermore, from the scanning fractograph in Fig. 5(b)– (d), it can be determined that there are quantities of aggregations

of precipitated phase and shrinkage cavity in the microstructure under the process without TMF (Fig. 5(b)). While, when the Up-TMF is added, the aggregation of precipitated phase still remains, and the shrinkage cavity begins to coalesce and to form the shrinkage cavity with a larger size (Fig. 5(c)). In addition, in the process of No-TMF or Up-TMF, the dimples are few and small, resulting in a sharp reduction of ductility in the alloy samples. Conversely, the Down-TMF can prominently reduce the aggregation of precipitated phase, and eliminate the shrinkage cavity. Moreover, under the process with Down-TMF, the size and the number of dimples are notably enhanced, which are distributed uniformly in the microstructure and connected with each other by the tear ridges (Fig. 5(d)). As a result, the ductility of alloy samples is greatly raised. Ultimately, optimization of microstructure and mechanical performance can be effectively obtained by the Down-TMF process.

Discussion

Simulation of travelling magnetic fields coupling with flow fields

The Ansoft-Maxwell software and Ansoft-CFX software were used together to calculate the coupling of the magnetic fields with flow fields, by importing the average magnetic force density of each position in the ZL205A alloys melt into the unidirectional solidification process. Then, the melt flows during the unidirectional solidification in the same time period with different TMF
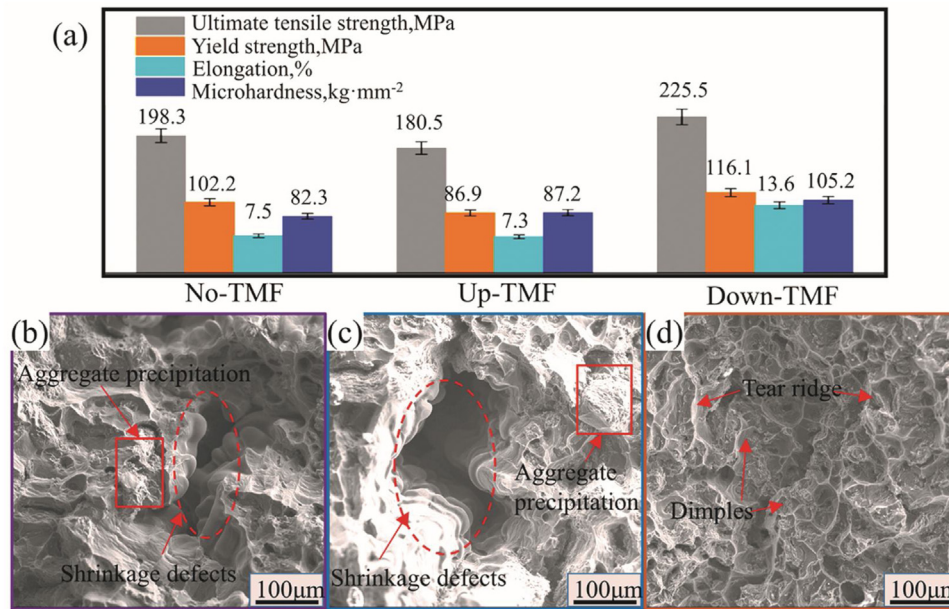
Fig. 5. Performance testing results: (a) Performance statistics. (b), (c) and (d) are scanning fractograph for No–TMF, Up–TMF and Down–TMF, respectively.
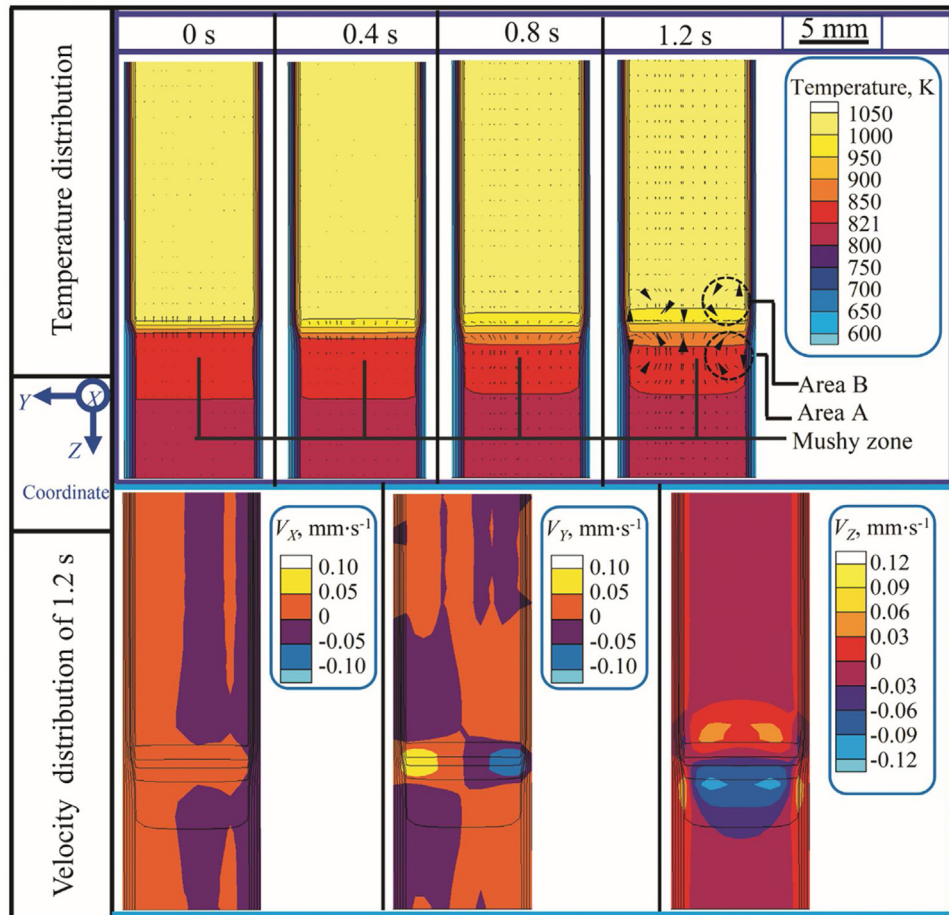

Fig. 6. The melt flows from 0 s to 1.2 s and the flow velocities after 1.2 s with No-TMF processing.

process conditions were obtained for comparative study as shown in Figs. 6– 8. It can be observed from Fig. 6 that, weak upward (Area A) and downward (Area B) melt flows are produced by gravity, buoyancy and Marangoni forces [25,26] at the front of solid-liquid interface during the solidification process without TMF, which will limit to some extent the transfer of latent heat from solid-liquid interface to a higher temperature region far from the mushy zone. Instead, TMF can produce strong, long-range and directional melt flows to further influence the distribution of temperature in mushy zone (Figs. 7 and 8). Noteworthily, the melt flows simulated in
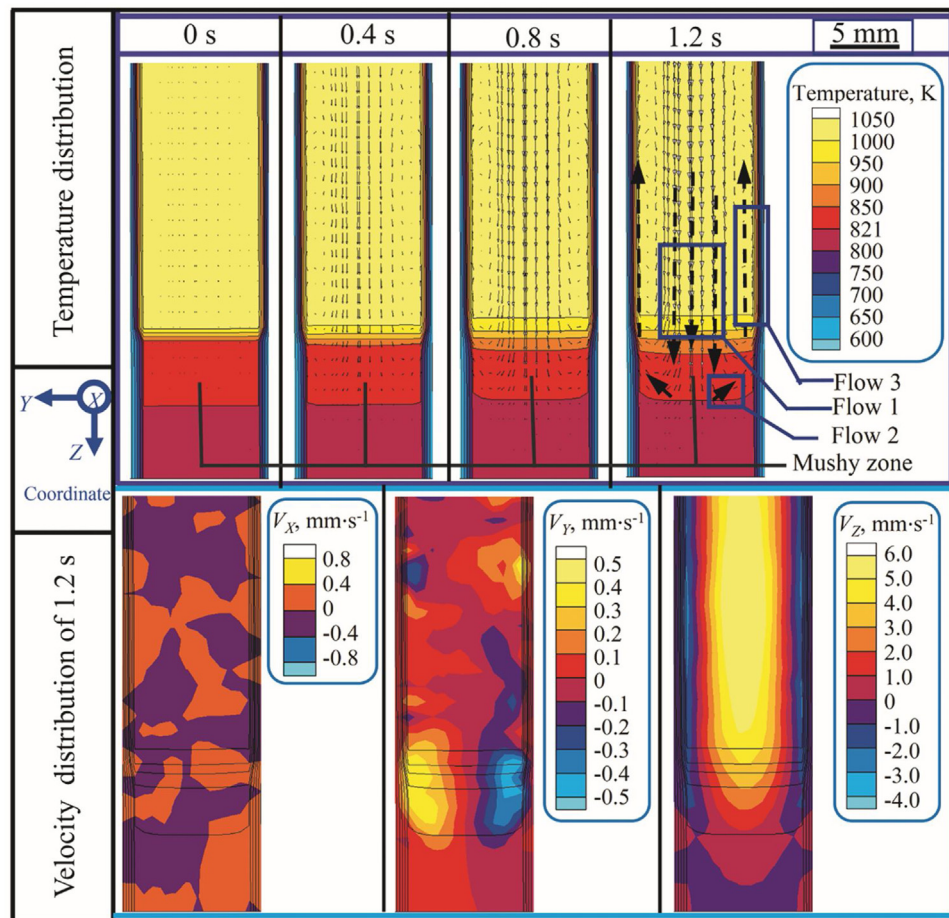
Fig. 7. The melt flows from 0 s to 1.2 s and the flow velocities after 1.2 s with Up-TMF processing.

Figs. 7 and 8 were generated by the combination of gravity, buoyancy, Marangoni forces and the Lorentz forces [25,26]. Specifically, as shown in Fig. 7, the long-range and rapid downward flows (Flow 1) from higher temperature region to the solid-liquid interface, the weak upward flows (Flow 3), and the weak radial flows (Flow 2) are generated in the alloy melt by the Up-TMF process. It can be determined that the maximum velocity of the longitudinal melt flows is 6 mm·s⁻¹, while the maximum velocity of the radial melt flows is 0.5 mm·s⁻¹. By focusing on the center of the mushy zones along the radial direction, the strong longitudinal melt flows as Flow 1 (Fig. 7) from distant alloy melt to the mushy zones, will transfer the melt with higher temperature to the solid-liquid interface to inhibit the longitudinal transport of latent heat produced at the center. In this case, the latent heat can only escape from the center by the radial transport (Flow 2). Additionally, the latent heat generated at the sidewalls can move upward by Flow 3, making the temperature at sidewalls decreased relatively quickly. Eventually, a concave solid-liquid interface can be formed by the combination of all the melt flows. Conversely, the long-range and rapid upward flows (Flow 4), the long-range and weak downward flows (Flow 6), and the weak radial flows (Flow 5) are formed in the alloy melt by the Down-TMF process (Fig. 8). Under the circumstances, the combination of all the melt flows can facilitate the longitudinal transport of latent heat from solid-liquid interface to the higher temperature region, but impede the radial transport from center to the sidewalls, so as to induce a flat or convex solid-liquid interface. During the solidification process, the morphology and the movement of the solid-liquid interface will cause a series of influences on the distribution the heat and solute. Specifically, solid-liquid interface of different shapes can produce the latent heat at different positions, causing a change in the distribution of heat. Furthermore, during the growth process of the solid-liquid interface with different shapes, the mushy zones will capture the surrounding solutes, so as to change the distribution of solutes. Therefore, although the strong melt flows can be generated by the different TMF process, the distribution of heat and solute will be different, and the solidification behavior and the microstructure can be altered accordingly [28,29]. The results of melt flows are consistent with the previous studies on Al-5 wt.% Cu alloys model [27]. However, the velocities of melt flows in ZL205A alloys are a little larger than them in Al-5 wt.% Cu alloys model. This is because that the flow rates of various precipitated phases are different under TMF or gravity process in ZL205A alloys. Besides, the influence of TMF at different stage of solidification process will be diverse. Based on this point, the in-depth research was conducted on the effects of TMF on the microstructure at each stage of solidification process, as well as the shrinkage defects and mechanical properties as follow.

Mechanism of TMF on the precipitation phase and matrix phase α-Al

Considering the multi-element and multi-phase in ZL205A alloys, the solidification paths and the phase diagrams were calculated by the Pandat software, and the results are shown in Fig. 9. By combining Fig. 9(a) and (b), it can be clearly illustrated that the Al₃Ti phase is the first phase to form at 1009 K in the ZL205A alloys, so as to become the nucleation particles for the formation of α-Al at 923 K [42]. As the temperature decreases to 898 K, the Al₆Mn phase begins to form. Subsequently, with the continued decrease of temperature to 821 K, another eutectic reaction begins to take
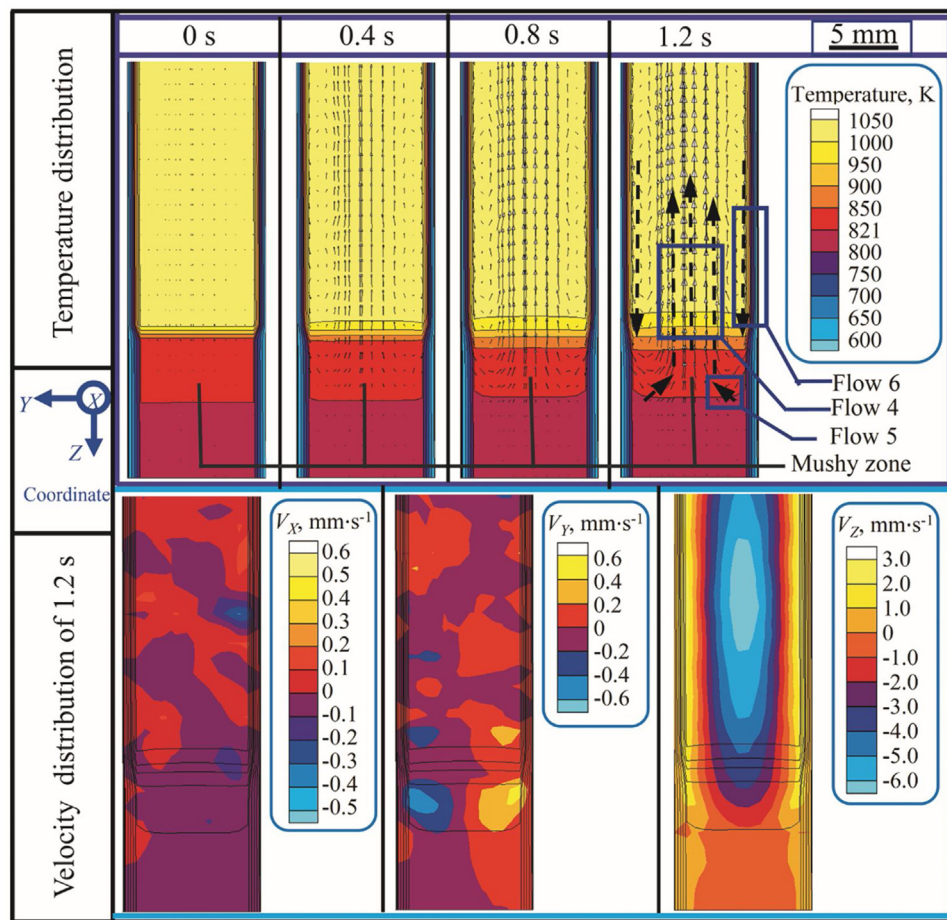
Fig. 8. The melt flows from 0 s to 1.2 s and the flow velocities after 1.2 s with Down-TMF processing.

place, resulting in the formation of Al_2Cu phase. Accordingly, the precipitation sequence of phases during the solidification of ZL205A alloys can be obtained. Specifically, the Al_3Ti is the first to appear, followed by α-Al, then the Al_6Mn, and finally the Al_2Cu. In order to analyze the effects of TMF on the microstructure of ZL205A alloys comprehensively, each step and each phase during the solidification process according to the precipitation sequence was studied intensively.

Firstly, the Al_3Ti was analyzed separately, because it preferentially formed over the matrix phase α-Al at the first stage of solidification process. Without the TMF process, the melt flows with less velocity (maximum velocity is about 0.12 mm s^{-1}) in the opposite directions (Area A and Area B in Fig. 6) will cause the Al_3Ti particles dissolved out during the solidification to aggregate and grow up due to the restriction of melt flows from solidi-liquid interface to the distant melt. As a result, both the size and the quantity of Al_3Ti with a flake shape are large (Fig. 2(a)). While, the addition of TMF can change the formation and growth behavior of Al_3Ti particles, from the perspective of changes in Gibbs free energy. On the basis of the classical theory of thermodynamics, the variations of Gibbs free energy can produce supply the driving force for the nucleation of Al_3Ti crystals, while the changes of interfacial free energy result in resistance for it [43,44], as follows:

$$\Delta G_g = \tau \cdot S_g + V \cdot \Delta G_V \tag{3}$$

where ΔG_g, τ and ΔG_V respectively denote the changes of Gibbs free energy, interfacial free energy and volume free energy during the solid-liquid phase transformation process of Al_3Ti. S_g denotes the superficial area of Al_3Ti crystal nucleus, and V denotes the

volume of the crystal nucleus. Further, the radius R of the Al_3Ti nucleated crystal was used to convert Eq. (3) to:

$$\Delta G_g = \tau \cdot 4\pi R^2 + (4/3)4\pi R^3 \Delta Gv \tag{4}$$

And the critical nucleation radius R_c of Al_3Ti can be obtained as:

$$R_c = -2\tau/\Delta Gv. \tag{5}$$

The addition of the TMF process can change the Gibbs free energy by adding the extra energy [44–46], so as to convert the Eqs. (3) and (5) to:

$$\Delta G_g = \tau \cdot S_g + V \cdot \Delta G_V + V \cdot \Delta G_{TMF}, \tag{6}$$

$$R_{TMF} = -2\tau/(\Delta G_V + \Delta G_{TMF}), \tag{7}$$

where ΔG_{TMF} is the magnetic free energy added by TMF process, and R_{TMF} is the critical nucleation radius of Al_3Ti with the TMF process. Obviously, the value of R_{TMF} is less than R_c, which theoretically demonstrates that TMF can effectively decrease the critical nucleation radius of Al_3Ti, in turn to refine its grain size. Nevertheless, with the Up-TMF process, the Flow 1 in Fig. 7 promotes the alloy melt flowing from higher temperature region to the mushy zone, so as to drastically impede the transfer of solute and latent heat from the mushy zone to other regions, resulting in a corresponding aggregation of the Al_3Ti particles, as well as a decrease of temperature gradient G_T-(Up-TMF) and undercooling temperature ΔT_k-(Up-TMF) at the front of solid-liquid interface [27]. In this case, the refinement of Al_3Ti and the solid solubility of Al_3Ti particles in the subsequent matrix phase α-Al will subject to certain limitations, so that some Al_3Ti will still appear in the microstructure and grow up to become the morphology with
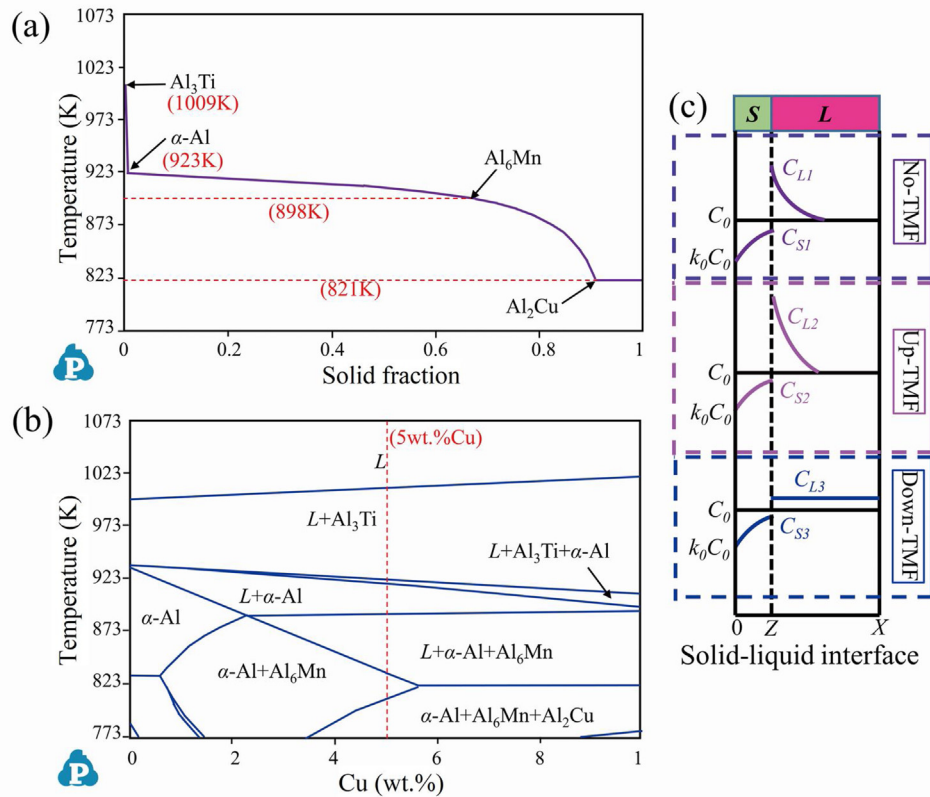
Fig. 9. Schematic diagrams of solidification process under different conditions: (a) Solidification path for ZL205A alloys. (b) Phase diagram curves of ZL205A alloys. (c) Distribution of solutes at the solid-liquid interface.

a certain size and a flake shape (Fig. 2(b)). On the contrary, in the process with Down-TMF, the Flow 4 in Fig. 8 facilitates the transfer of latent heat from the mushy zone to higher temperature regions, further to decrease the accumulation of Al_3Ti particles, leading to an increase of temperature gradient G_T-(Down-TMF) and under-cooling temperature ΔT_k-(Down-TMF) [27]. In the circumstances, the refinement of Al_3Ti can be greatly improved, as well as the solid solubility of Al_3Ti particles in the subsequent matrix phase α-Al. As a result, the appearance of Al_3Ti with a certain size and flake shape in the microstructure is reduced or eliminated (Fig. 2(c)). Addition-ally, comparing with the No-TMF process, the directional melt flows with higher velocity (the maximum velocity is about 6 mm·s^{-1} in both the Down-TMF process and the Up-TMF process) can stir the alloy melt to uniform the distribution of Al_3Ti particles, further to reduce the aggregation of them to some extent [30,47]. Ulti-mately, in comparison with the process without TMF, the addition of TMF can refine the size of Al_3Ti phase and uniform the distri-bution of them. Additionally, due to the increase of undercooling temperature ΔT_k, Down-TMF can enhance the solid solubility of Al_3Ti particles in the matrix phase α-Al [27], in turn to reduce or even eliminate the appearance of Al_3Ti with a certain size and flake shape in the microstructure. Inversely, Up-TMF has less effects on the solid solubility improvement of Al_3Ti, so that the Al_3Ti with a certain size and flake shape can still exist, although the size and dis-tribution of Al_3Ti have been decreased and uniformed to a certain extent.

Similarly, the subsequent precipitated phase Al_6Mn and Al_2Cu occurred with the formation of matrix phase α-Al can also be influ-enced by TMF at the later stage, which are mainly manifested in the variations of formation, distribution and the solid solubility of Mn and Cu element in the matrix phase α-Al. From the Fig. 9(b), it can be determined that accompanied with the formation of matrix phase α-Al and the movement of solid-liquid interface, the excess

solutes of Mn and Cu elements produced from α-Al will cause the generation of the Al_6Mn and Al_2Cu phases [48,49]. While, the TMF process can largely change the distribution of the solutes (Mn and Cu) around the solid-liquid interface for the transient state during the unidirectional solidification as shown in Fig. 9(c). According to the relevant Refs. [27,50,51], the solidification behavior at a tran-sient state can be expressed as:

$$k_0 = C_S/C_L, \tag{8}$$

$$T_L = T_0 - mC_0\{1 + [(1-k_0)/k_0]\exp(-v_gZ/D_d)\}, \tag{9}$$

where the C_L and C_S are the solute concentrations in liquid phase and solid phase at the solid-liquid interface for the transient state respectively, k_0 is the solute partition coefficient ($k_0 < 1$), T_0 is the melting temperature of the pure solvent, T_L is the instantaneous melting temperature of the alloy at solid-liquid interface in the transient state, Z is the position of solid-liquid interface, m is the slope of liquid phase, v_g is the rate of interface movement and D_d is the diffusion coefficient of solute in liquid phase. Consequently, Down-TMF can effectively transport the excess solutes (Mn and Cu) and the latent heat from the solid-liquid interface to the higher temperature and lower solute concentration region far from the mushy zone (Fig. 8). Therefore, the instantaneous solute concen-tration in the liquid phase C_L-(Down-TMF) will decrease to the value less than C_L-(No-TMF) (Fig. 9(c)), while the C_S-(Down-TMF) and C_S-(No-TMF) in the solid phase can be regarded as equal at the point. Eventually, by the Eqs. (8) and (9), the instantaneous solute partition coefficient k_0-(Down-TMF) and T_L-(Down-TMF) will be larger than k_0-(No-TMF) and T_L-(No-TMF), respectively. Addition-ally, combining with the effective transfer of the latent heat from the solid-liquid interface to the higher temperature region with the Down-TMF process, a larger cooling rate can be obtained, so as to greatly increase the undercooling temperature ΔT_k-(Down-TMF).

Hence, adsorption of Cu and Mn atoms and the solid solubility of them in matrix phase α-Al will all be significantly enhanced [50–52], in turn to reduce the formation of Al_2Cu and Al_6Mn. Comparing with the No-TMF process, Down-TMF can effectively optimize and uniform the distribution of excess Cu and Mn elements in the alloys melt, and improve the solid solubility of them in the matrix phase α-Al, as well as reduce the formation and aggregation of Al_2Cu and Al_6Mn phase in the microstructure. However, in sharp contrast to Down-TMF process, the Up-TMF will generate the opposite directional melt flows during the unidirectional solidification process, so that the k_0-(Up-TMF) and ΔT_k-(Up-TMF) are decreased, resulting in negative effects on the uniform distribution of Cu and Mn elements, accordingly, it will increase the formation and aggregation of Al_2Cu and Al_6Mn phase.

Finally, with respect to the matrix phase α-Al, the growth behavior and morphology of them can be analyzed. As shown in Fig. 6, in the process without TMF, the weak upward melt flows (Area A) can enhance the transport of solute and latent heat to the regions distant from the solid-liquid interface to some extent, further to promote the growth of matrix phase α-Al along the direction of temperature gradient. Nevertheless, the weak downward melt flows (Area B) will inhibit these results. Consequently, the growth direction of matrix phase α-Al becomes disordered, and certain numbers of secondary dendrites begin to form. Contrastively, Down-TMF can significantly promote the transmission of solute and latent heat from the solidification front to the distant regions (Fig. 8), further to greatly facilitate the growth consistency of primary α-Al dendrites growing along the <001> crystal orientation and reduce the secondary dendrites [53]. In this case, the overlaps between dendrites can be decreased or eliminated. On the contrary, Up-TMF will drastically restrict the transmission of solute and latent heat from the solidification front to the distant regions, but promote the transmission from center to the sidewalls, in turn, it will cause the primary α-Al dendrites to deflect and cause the growth of the secondary dendrites to be increased. In regard to the morphology of matrix phase α-Al, the dendrite size of matrix phase α-Al can be qualitatively characterized by using the primary dendrite arm spacing λ_1 and secondary dendrite arm spacing λ_2, as follows [54,55]:

$$\lambda_1 = 4.3(\Delta T_0 D_d \Gamma/k_0)^{1/4} \cdot G_T^{-1/2} \cdot v_g^{-1/4}, \tag{10}$$

$$\lambda_2 = 7.5 t_l^{0.39}, \tag{11}$$

where ΔT_0 is solidification intervals, Γ is the Gibbs-Thomson coefficient, and t_l is the local solidification time at solid-liquid interface. From Eqs. (8) and (9), it can be concluded that Down-TMF can significantly increase the k_0-(Down-TMF), G_T-(Down-TMF) and ΔT_k-(Down-TMF), so that the λ_1 and λ_2 can be decreased accordingly (Eqs. (10) and (11)), that is, the Down-TMF can effectively refine the grain and dendrite size of matrix phase α-Al. However, the Up-TMF processing can decrease the k_0-(Up-TMF), G_T-(Up-TMF) and ΔT_k-(Up-TMF), resulting in an increase of λ_1 and λ_2, finally the grain and dendrite size of matrix phase α-Al will be enlarged contrast to the Down-TMF process [8]. Additionally, compared with the process without TMF, Up-TMF can still reduce dendrite size to some extent, because of a certain positive effect on the uniform distribution and refinement of Al_3Ti, which are the nucleation particles of matrix phase α-Al.

Consequently, comparing with the process without TMF, Down-TMF and Up-TMF can continuously influence the solidification behavior and regulate the mushy zone at different solidification stages. Therefore, the formation, the morphology and the distribution of microstructure in ZL205A alloys, including the precipitated phase (Al_3Ti, Al_6Mn and Al_2Cu) and matrix phase α-Al, are all affected by the strong long-range directional melt flows generated by TMF. What is noteworthy is that, the different results induced by
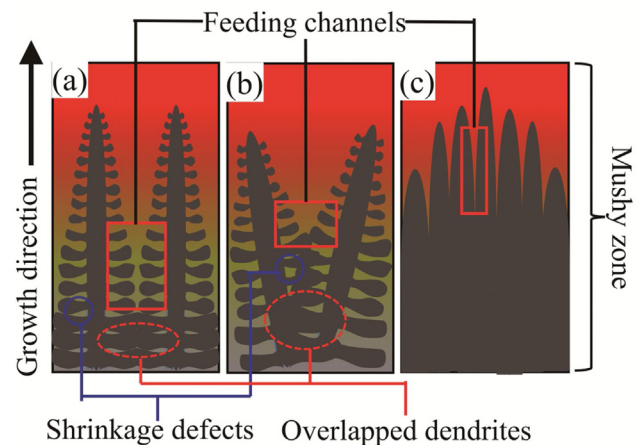

Fig. 10. Schematic diagrams of the feeding behavior in the different processes: (a) No-TMF. (b) Up-TMF. (c) Down-TMF.

Down-TMF and Up-TMF is mainly due to the different direction of magnetic force and melt flows produced by TMF. Additionally, the effects of TMF on microstructural evolution are dissimilar at the different stages unidirectional solidification, due to the solidification sequence of multi-element ZL205A alloys with multi-phase.

Mechanism of TMF on the shrinkage defects

In order to analyze the shrinkage behavior of alloys, the unidirectional solidification models in different conditions were established as shown in the Fig. 10. Under the circumstances, the cross sections of the feeding channels are regarded as the circular sections with the radius R, which decreases as the volume fraction of solid phase increases. Without the TMF process, due to the comparatively low velocity of melt flows (the maximum velocity is about 0.12 mm s^{-1}), the alloy melt in the mushy zone is difficult to quickly enter the feeding channels in a limited time, so that the feeding rate will be less than the solidified rate, resulting in a decrease of feeding capacity during the unidirectional solidification. Therefore, the shrinkage defects are easier to form without the TMF process (Fig. 10(a)). By adding the TMF process, the melt flows with larger velocities (with a maximum velocity is about 6 mm s^{-1} in both the Down-TMF and Up-TMF process) can accelerate the alloy melt entering into the feeding channels and decline the feeding time, further to enhance the feeding capacity and remove the shrinkage defects. In addition, based on the dynamic conditions in the mushy zone during the unidirectional solidification process, TMF can affect the feeding pressure in the feeding channels, which can influence the feeding behavior accordingly, as follows [9,56]:

$$\Delta P_s = \sigma \cdot R_k^{-1}, \tag{12}$$

$$R_k = R(L_0^2 - R_0^2)^{1/2} \cdot L_0^{-1}. \tag{13}$$

where ΔP_s is the increased pressure generated by surface tension, σ is the surface tension of alloy melt in the feeding channels. In addition, R_k, R, R_0 and L_0 denote respectively the curvature radius, the radius of cross section, the radius of initial position and the total length for the feeding channels. Currently, the value of R_0 is far less than L_0 in the feeding channels, so that the Eqs. (12) and (13) can be combined and changed as:

$$\Delta P_s = \sigma \cdot R^{-1}. \tag{14}$$

Furthermore, the external volume force including the gravity and magnetic force will induced the increase of feeding pressure,

while the growth of dendrites will result in a reduction of them, specially, they can be expressed as [9,56]:

$$\Delta P_v = (\rho g + f_m) \cdot L. \tag{15}$$

$$\Delta Pd = \int_0^L 8u\eta R^{-2} dL \tag{16}$$

where ΔP_v denotes the increased pressure by external volume force, ρ is the density of ZL205A alloy melt, g is the gravity coefficient, f_m is the magnetic force density along the feeding channels generated by TMF, L is the maximum length of the feeding capacity in the feeding channels, ΔP_d is the decreased pressure with the growth of dendrites, u is the feeding rate of alloy melt in feeding channels and η is the viscosity coefficient of alloy melt. Here, the feeding process can be considered as a continuous process, so that the Eq. 16 can be converted to:

$$\Delta P_f = 8u\eta R^{-2} L. \tag{17}$$

Consequently, based on the law of conservation of energy, it can be obtained that [56]:

$$\Delta P_0 + \Delta P_s + \Delta P_v - \Delta P_f = 0. \tag{18}$$

where the ΔP_0 denotes the difference of static pressure along the feeding channels. By combining the Eqs. (14)– (18), it can be intuitively deduced that by increasing the f_m, i.e., adding the TMF process, the length L representing the feeding capacity can be enhanced. Accordingly, TMF can significantly promote both the feeding rate and feeding pressure, so as to effectively improve the feeding capacity of alloy melt and reduce shrinkage defects of ZL205A alloys with large solidification intervals and multi-phase. Noteworthily, these deductions are based on an assumption that the feeding channels are not affected by the TMF process, due to that the feeding channels can play a crucial role in this process. However, the different directional TMF can indeed cause different effects on the feeding channels as discussed above. Especially, Down-TMF can improve the growth consistency of matrix phase α-Al along the direction of temperature gradient, while reduce the secondary dendrite and overlaps between dendrites, resulting in a further enhancement of feeding capacity and effective elimination of shrinkage defects (Fig. 10(c)). However, Up-TMF will promote the formation of secondary dendrite and overlaps between dendrites, deflect and disorder the growth of matrix phase α-Al, so that the feeding channels are badly blocked. Eventually, the feeding capacity tends to decline and the shrinkage defects are easier to form and accumulate, although Up-TMF can accelerate the melt flows and increase feeding pressure (Fig. 10(b)).

Mechanism of the coupling of TMF on the mechanical performance

The microstructural evolution and variations of shrinkage defects produced by TMF can significantly influence the mechanical performance. Comparing with No-TMF process, by adding the Up-TMF, the distribution of preferential precipitated phase Al$_3$Ti can be uniformed, and the size of them can be refined. Additionally, the solid solubility of Al$_3$Ti particles in the matrix phase α-Al can be increased. Therefore, the tensile strength and hardness should have been relatively enhanced to a certain extent [40,41]. However, in regard to the subsequent precipitation phase including Al$_2$Cu and Al$_6$Mn, Up-TMF has negative effects on them. Especially, Up-TMF increases the formation and aggregation of them. Moreover, it deceases the solid solubility of Cu and Mn in the matrix phase α-Al. As a result, the tensile strength and hardness are negatively affected. Besides, Up-TMF seriously deflects and disorders the growth of matrix phase α-Al, and promotes the abundant formation of secondary dendrite and overlaps between dendrites,

resulting in more formation and aggregation of shrinkage defects [57,58]. All these changes make the tensile strength decrease relatively comparing with the process without TMF, and reduce the ductility of alloys. Contrastively, Down-TMF can greatly reduce the formation and aggregation of all the precipitated phases including the Al$_3$Ti, Al$_2$Cu and Al$_6$Mn, further to uniform the distribution of them. Moreover, Down-TMF can largely increase the solid solubility of Al$_3$Ti particles, Cu and Mn elements in the matrix phase α-Al, and efficiently improve the growth consistency of matrix phase α-Al along the direction of temperature gradient, as well as effectually decrease the formation of secondary dendrite and overlaps between dendrites, in turn to significantly eliminate the shrinkage defects. Ultimately, the tensile strength, the ductility and the hardness of alloys can be enormously improved by coupling the Down-TMF with the unidirectional solidification process. Additionally, in this work, the specific TMF parameters and the overheating temperature have been selected, which will also result in a series of influences on the microstructures, defects and mechanical performances, and will be the future research directions for the TMF casting process.

Conclusions

In this paper, the microstructure and mechanical performance of ZL205A alloys were optimized by coupling TMF with unidirectional solidification, and the mechanisms were comprehensively studied by combining experiments with simulations. Accordingly, the following conclusions can be drawn:

TMF coupled with unidirectional solidification can alter the solidification behavior, including the microstructural evolution and feeding behavior, further to influence the mechanical performance of ZL205A alloys, by generating the strong directional melt flows. Additionally, the effects of TMF on the microstructural evolution are various at the different stage of solidification process according to the precipitation sequence. Furthermore, the effects are different by the different directional TMF.

Down-TMF can refine and uniform the microstructure of ZL205A alloys, reduce the formation of all the precipitation, promote the growth consistency of matrix phase α-Al growing along the <001> crystal orientation, decline the secondary dendrites and overlaps between dendrites, and eliminate the shrinkage defects. Contrastively, Up-TMF increases the formation of Al$_6$Mn, Al$_2$Cu, secondary dendrites, overlaps between dendrites, and shrinkage defects, resulting in deflection and disorder for the growth of matrix phase α-Al, although it can refine the α-Al and reduce the formation of Al$_3$Ti with blocky morphology.

Down-TMF can significantly enhance the mechanical performance. Specifically, it can increase the ultimate tensile strength, yield strength, elongation and hardness from 198.3 MPa, 102.2 MPa, 7.5 % and 82.3 kg mm^{-2} without TMF to 225.5 MPa, 116.1 MPa, 13.6 % and 105.2 kg mm^{-2}, as well as the ductility of ZL205A alloys. While Up-TMF will result in negative impacts on the overall mechanical performance, despite it can increase the hardness to some extent.

Acknowledgements

References

[1] D.F. Du, L. Hou, A. Gagnoud, Z. Ren, Y. Fautrelle, G.H. Cao, X. Li, J. Alloys. Compd. 588 (2014) 190–198.
[2] J.M. Rosalie, L. Bourgeois, Acta Mater. 60 (2012) 6033–6041.

[3] L. Gao, X.Q. Ou, S. Ni, K. Li, Y. Du, M. Song,Mater. Sci. Eng. A 762 (2019), 138091.
[4] G. Liu, J. Sun, C.W. Nan, K.H. Chen, Acta Mater. 53 (2005) 3459–3468.
[5] Z.M. Gao, W.Q. Jie, Y.Q. Liu, H.J. Luo, Acta Mater. 127 (2017) 277–286.
[6] B. Li, Y.F. Shen, W.Y. Hu, Mater. Des. 32 (2011) 2570–2582.
[7] M.N. Patel, D. Qiu, G. Wang, M.A. Gibson, A. Prasad, D.H. Stjohn, M.A. Easton, Scr. Mater. 178 (2020) 447–451.
[8] A. Shaga, P. Shen, L.G. Xiao, R.F. Guo, Y.B. Liu, Q.C. Jiang, Mater. Sci. Eng. A 708 (2017) 199–207.
[9] Q.L. Li, Y.S. Zhang, Y.F. Lan, Y.X. Zhang, T.D. Xia,J. Alloys. Compd. 831 (2020), 154739.
[10] H. Elhadari, H. Patel, D. Chen, W. Kasprzak, Mater. Sci. Eng. A 528 (2011) 8128–8138.
[11] J. Delahaye, J.T. Tchuindjang, J. Lecomte-Beckers, O. Rigo, A. Habraken, A. Mertens, Acta Mater. 175 (2019) 160–170.
[12] H. Neumann-Heyme, K. Eckert, C. Beckermann, Acta Mater. 140 (2017) 87–96.
[13] X. Li, Q. Cai, B. Zhao, Y. Xiao, B. Li, J. Alloys. Compd. 675 (2016) 201–210.
[14] S. Liu, D. Zhang, J. Xiong, C. Chen, T. Song, L. Liu, S. Huang, J. Alloys. Compd. 781 (2019) 873–882.
[15] X. Zhang, L. Huang, B. Zhang, Y. Chen, S. Duan, G. Liu, C. Yang, F. Liu, Mater. Sci. Eng. A 753 (2019) 168–178.
[16] J. Gao, M. Han, A. Kao, K. Pericleous, D.V. Alexandrov, P.K. Galenko, Acta Mater. 103 (2016) 184–191.
[17] H. Wei, F. Xia, S. Qian, M. Wang, J. Mater, Proc. IEEE Int. Symp. Signal Proc. Inf. Tech. 240 (2017) 344–353.
[18] F. Wang, D. Eskin, J. Mi, C. Wang, B. Koe, A. King, C. Reinhard, T. Connolley, Acta Mater. 141 (2017) 142–153.
[19] C. Lin, S. Wu, S. Lü, P. An, L. Wan, J. Alloys. Compd. 568 (2013) 42–48.
[20] X.U. Bin, R.U.I. Zhi-yuan, Adv. Mater. Res. 1061 (2015) 465–470.
[21] L.Q. Zhang, W.F. Tan, H. Hu, Heat Mass Transf. 52 (2016) 1131–1138.
[22] H. Liu, Y. Gao, L. Qi, Y. Wang, J.F. Nie, Metall. Mater. Trans. A 46 (2015) 3287–3301.
[23] D.V. Alexandrov, P.K. Galenko, Phys. Usp. 57 (2014) 771.
[24] M.H. Avnaim, B. Mikhailovich, A. Azulay, A. Levy, Int. J. Heat Fluid Flow 69 (2018) 9–22.
[25] K. Zhang, Y. Li, Y. Yang, J. Mater, Sci. Technol. 48 (2020) 9–17.
[26] Y. Zhao, K. Wang, S. Yuan, Y. Ma, G. Li, Q. Wang, J. Mater, Sci. Technol. 46 (2020) 127–135.
[27] L. Luo, L.S. Luo, R.O. Ritchie, Y.Q. Su, B. Wang, L. Wang, R.R. Chen, J.J. Guo, H.Z. Fu, J. Mater, Sci. Technol. 61 (2021) 100–113.
[28] E. Liotti, A. Lui, S. Kumar, Z. Guo, C. Bi, T. Connolley, P. Grant, Acta Mater. 121 (2016) 384–395.
[29] Y.Z. Li, N. Mangelinck-Noel, G. Zimmermann, L. Sturz, H. Nguyenthi,J. Alloys. Compd. 836 (2020), 155458.
[30] G. Zimmermann, C. Pickmann, M. Hamacher, E. Schaberger-Zimmermann, H. Neumann-Heyme, K. Eckert, S. Eckert, Acta Mater. 126 (2017) 236–250.
[31] D. Ruvalcaba, R. Mathiesen, D. Eskin, L. Arnberg, L. Katgerman, Acta Mater. 55 (2007) 4287–4292.
[32] M. Dong, T. Liu, X. Guo, Y. Liu, S. Dong, Q. Wang,Mater. Sci. Eng. A 785 (2020), 139377.
[33] B. Nawaz, X. Long, Z. Yang, J. Zhao, F. Zhang, J. Li, Mater. Sci. Eng. A 759 (2019) 11–18.
[34] Z.Y. Li, X.F. Qi, L.J. Liu, G.S. Zhou, J. Cryst. Growth 484 (2018) 78–85.
[35] P. Schwesig, M. Hainke, J. Friedrich, G. Mueller, J. Cryst. Growth 266 (2004) 224–228.
[36] H. Yan, T. Gao, H. Zhang, J. Nie, X. Liu, J. Mater. Sci. Technol. 35 (2019) 374–382.
[37] X. Yang, J. Zhu, W. Li, J. Mater. Sci. Technol. 31 (2015) 1320–1328.
[38] B. Lin, R. Xu, H. Li, W. Zhang, J. Mater. Sci. Technol. 34 (2018) 1447–1459.
[39] A.P. Boeira, I.L. Ferreira, A. Garcia, Mater. Des. 30 (2009) 2090–2098.
[40] E. Cadirli, Met. Mater. Int. 19 (2013) 411–422.
[41] N.J. Petch, J.Iron Steel Inst. 174 (1953) 25–28.
[42] Z. Liu, N. Cheng, Q. Zheng, J. Wu, Q. Han, Z. Huang, J. Xing, Y. Li, Y. Gao, Mater. Sci. Eng., A 710 (2018) 392–399.
[43] C.D. Zhao, J.S. Li, Y.X. He, J.X. Wang, W.Y. Wang, H.C. Kou, J. Wang,J. Alloys. Compd. 820 (2020), 153407.
[44] T. Hou, Z. Li, K. Wu, H. Lin, Y. Li, G. Zhang, W. Liu, Acta Mater. 167 (2019) 71–79.
[45] R. Xin, K. Wu, G. Zhang, T. Hou, G. Ma, W. Qiao, H. Zhao, J. Mater. Sci. Technol. 34 (2018) 786–793.
[46] B. Dong, T. Hou, K. Wu, Z. You, Z. Li, G. Zhang, Mater. Lett. 240 (2019) 66–68.
[47] H. Sato, T. Murase, T. Fujii, S. Onaka, Y. Watanabe, M. Kato, Acta Mater. 56 (2008) 4549–4558.
[48] Y. Dong, Y. Shuai, T. Zheng, J. Cao, C. Chen, J. Wang, Z. Ren, J. Mater. Sci. Technol. 39 (2020) 113–123.
[49] Y. Zhao, B. Zhang, H. Hou, W. Chen, M. Wang, J. Mater. Sci. Technol. 35 (2019) 1044–1052.
[50] Y. Xu, D. Casari, Q. Du, R.H. Mathiesen, L. Arnberg, Y. Li, Acta Mater. 140 (2017) 224–239.
[51] F. Sá, O.L. Rocha, C.A. Siqueira, A. Garcia, Mater. Sci. Eng. A 373 (2004) 131–138.
[52] L. Wang, W. Lu, Q. Hu, M. Xia, Y. Wang, J. Li, Acta Mater. 139 (2017) 75–85.
[53] S. Li, C. Wu, K. Sassa, S. Asai, Mater. Sci. Eng., A 422 (2006) 227–231.
[54] Y. Zhang, X. Miao, Z. Shen, Q. Han, C. Song, Q. Zhai, Acta Mater. 97 (2015) 357–366.
[55] Y. Wang, S. Li, Z. Liu, H. Zhong, L. Xu, H. Xing, J. Mater. Sci. Technol. 35 (2019) 1309–1314.
[56] Z. Gao, W. Jie, Y. Liu, Y. Zheng, H. Luo, J. Alloys. Compd. 797 (2019) 514–522.
[57] M. Schöbel, R. Fernández, R. Koos, J. Bernardi, J. Alloys. Compd. 775 (2019) 617–627.
[58] H. He, Y. Yi, S. Huang, Y. Zhang, J. Mater. Sci. Technol. 35 (2019) 55–63.